Electron correlations in the cubic paramagnetic perovskite math xmlns="http://www.w3.org/1998/Math/MathML">mi>Sr/mi>mo>(/mo>mi mathvariant="normal">V/mi>mo>, /mo>mi>Mn/mi>mo>)/mo>msub>mi mathvariant="normal">O/mi>mn>3/mn>/msub>/math>: Results from fully self-consistent self-energy embedding calculations

Chia-Nan Yeh, Sergei Iskakov, Dominika Zgid, and Emanuel Gull

Electron correlations in cubic paramagnetic perovskite Sr(V,Mn)O$_3$ - Results from fully self-consistent self-energy embedding calculations.

Chia-Nan Yeh,[1] Sergei Iskakov,[1] Dominika Zgid,[2, 1] and Emanuel Gull[1]

[1]*Department of Physics, University of Michigan, Ann Arbor, Michigan 48109, USA*
[2]*Department of Chemistry, University of Michigan, Ann Arbor, Michigan 48109, USA*
(Dated: May 12, 2021)

In this work, we use the thermodynamically consistent and conserving self-energy embedding theory (SEET) to study the spectra of the prototypical undistorted cubic perovskites SrVO$_3$ and SrMnO$_3$. In the strongly correlated metallic SrVO$_3$ we find that the usual attribution of the satellite peaks at -1.8eV to Hund or Hubbard physics in the t_{2g} orbitals is inconsistent with our calculations. In the strongly correlated insulator SrMnO$_3$ we recover insulating behavior due to a feedback effect between the strongly correlated orbitals and the weakly correlated environment. Our calculation shows a systematic convergence of spectral features as the space of strongly correlated orbitals is enlarged, paving the way to a systematic parameter free study of correlated perovskites.

I. INTRODUCTION

The simulation of strongly correlated solids within a rigorous parameter-free ab-initio theory is one of the big challenges of modern quantum physics. The goal is to find approximate methods able to describe the complexities of the electronic structure problem while, at the same time, taking into account electron correlations accurately.

The distortionless cubic oxide perovskites SrVO$_3$ and SrMnO$_3$ form an ideal testbed for these theories [1–13]. Of particular interest is the single-particle excitation spectrum, which can be probed by photemission and inverse photoemission techniques and which, in diagrammatic techniques, is directly related to the imaginary part of the real frequency spectral function.

While the spectrum of both materials is well characterized experimentally, standard electronic structure methods such as the density functional theory (DFT) and GW are not able to reproduce it due to the missing correlations in their partially filled transition metal shells. For instance, in the LDA calculations, the t_{2g} quasiparticle bandwidth in SrVO$_3$ is too wide, and SrMnO$_3$ is metallic, rather than insulating.

Both materials are prototypes for density functional theory plus dynamical mean field theory (DFT+DMFT) simulations [1–6, 9, 10, 12, 13]. In its simplest variant, this method fits three to five near-Fermi-surface bands and introduces effective Hubbard and Hunds parameters that broaden, split and shift the band structure such that 'quasiparticle peaks' and 'Hubbard sidebands' can be identified. In DFT+DMFT, an empirical choice of $U = 5$ eV and $J = 0.68$ eV generates a characteristic three-peak structure in SrVO$_3$, with a 'satellite' peak near -1.8 eV and a strong quasiparticle feature, leading to spectra that are remarkably close to experiment and entirely due to Hubbard physics [1, 3, 12]. Sometimes, U and J parameters determined by constrained LDA (cLDA) [14] are used although these parameters could lead to less accurate results [2, 4–6]. Similarly, a parameter choice of $U = 5$ eV and $J = 0.6$ eV along with an extra static double counting shift beyond the fully

localized limit (FLL) by -2.0 eV turns SrMnO$_3$ into a correlated insulator [13].

More elaborate calculations, such as the ones performed using the G_0W_0+GW+EDMFT multitier scheme of Ref. [15–17], avoid choosing empirical parameter choice by resorting to a parameter-free cRPA [18] calculation together with an extended impurity solution using 'screened interactions' in Wannier-downfolded d bands. For SrVO$_3$, the G_0W_0+GW+EDMFT results show that a naive interpretation of the 'satellite' peak as Hubbard phenomenon is inconsistent with the calculated spectra and the authors find plasmon physics. However in contrast to the experiment, for SrMnO$_3$, in G_0W_0+GW+EDMFT the paramagnetic phase (PM) is found to be metallic.

Here, we evaluate the photoemission spectra of both SrVO$_3$ and SrMnO$_3$ using a parameter-free ab-initio self-energy embedding theory (SEET) without resorting to screened interactions, Wannier function downfolding, or a DFT functional dependent starting point. We obtain a diagrammatic solution of the entire system in a thermodynamically consistent and conserving fashion, approximating the exact Luttinger-Ward functional Φ of the solid [19–21]. Starting from a self-consistent GW solution, we disentangle the individual effects of correlations in physically relevant orbital subgroups by systematically adding correlation diagrams to Φ. We demonstrate that gradually adding non-perturbative terms on the local vanadium (V), manganese (Mn) t_{2g}, e_g, and oxygen (O) p orbitals leads to a systematic convergence of the results towards photoemission data.

The remainder of this paper will proceed as follows. In Sec. II we will introduce the method and the computational details. In Sec. IV we will discuss its application to SrVO$_3$ and in Sec. V to SrMnO$_3$. In Sec. VI we will present conclusions.

II. METHOD

We study the electronic structure of paramagnetic $SrVO_3$ and $SrMnO_3$ using SEET [22–24] based on the procedures described in Ref. [25], using GW [15, 25–28] as the weakly correlated 'outer' method for all orbitals and Exact Diagonalization (ED) [29, 30] as the 'inner' quantum impurity solver for the correlated orbitals. We emphasize that, in the present work, we iterate the SEET equations fully to self-consistency [24, 25] as shown in Fig. 1 (see Sec. II A for details). This ensures that the self-energy in the weakly correlated orbitals is adjusted to reflect the influence of the self-energy coming from the strongly correlated orbitals. Full self-consistency is essential for a Φ-derivable theory that respects thermo-dynamic consistency and conservation laws [19–21, 31], and will be needed to recover the insulating character of the PM phase of $SrMnO_3$.

Our implementation of SEET does not rely on low-energy projections of orbitals and interactions but instead is formulated in terms of the bare electronic structure Hamiltonian. No effective model parameters, double counting corrections, or other adjustable parameters are employed. Non-local screening is fully included at the level of GW. The method is controlled in the sense that as the correlated subspace is enlarged, all correlations of the electronic structure problem are gradually recovered.

A. Self-energy embedding theory

We study the periodic electronic structure Hamiltonian

$$H = \sum_{ij,\sigma} h_{ij}^0 c_{i\sigma}^\dagger c_{j\sigma} + \frac{1}{2} \sum_{ijkl,\sigma\sigma'} v_{ijkl} c_{i\sigma}^\dagger c_{k\sigma'}^\dagger c_{l\sigma'} c_{j\sigma}, \quad (1)$$

where $c_{i\sigma}^\dagger$ ($c_{i\sigma}$) are creation (annihilation) operators for the single-particle state with spin σ and multi-index i, which represents orbital i and crystal momentum $\mathbf{k}_i$. We use symmetrized atomic orbitals (SAO) [32] constructed from Gaussian Bloch orbitals as the orbital basis. h_{ij}^0 and v_{ijkl} are the standard single-particle and two-particle operators; for an explicit definition see e.g. Eq. 4 of Ref. [25].

As a starting point, we employ the GW approximation as a weakly correlated method to obtain the momentum-resolved Green's functions $(G^{GW})^\mathbf{k}$ and self-energies $(\Sigma^{GW})^\mathbf{k}$. In GW, $(\Sigma^{GW})^\mathbf{k}$ is a functional $\mathcal{F}_{GW}$ of $(G^{GW})^\mathbf{k}$,

$$(\Sigma^{GW})^\mathbf{k} = \mathcal{F}_{GW}[(G^{GW})^\mathbf{k}]. \quad (2)$$

Along with the Dyson equation

$$(G^{GW}(i\omega_n))^\mathbf{k} = \left[(i\omega_n + \mu) - h^{0,\mathbf{k}} - (\Sigma^{GW}(i\omega_n))^\mathbf{k}\right]^{-1}, \quad (3)$$

Eq. 2 implies a self-consistency between Σ^{GW} and G^{GW}, defining the so-called self-consistent GW (scGW) approximation. Corrections to GW occur at second order in the interaction, and therefore the method may become unreliable when applied to strongly interacting systems.

SEET includes non-perturbative corrections to the GW self-energy diagrams within subsets of potentially strongly correlated orbitals. Here, we choose as the strongly correlated subsets M disjoint groups of local orbitals close to the Fermi energy E_F, labeled by $A_1 \ldots, A_M$.

SEET modifies the self-energy of Eq. 2 [23]

$$(\Sigma^{\text{SEET}})_{ij}^\mathbf{k} = (\Sigma^{\text{weak}})_{ij}^\mathbf{k}$$
$$+ \sum_{\lambda=1}^M \left[(\Sigma_{A_\lambda}^{\text{non-pert}})_{ij} - (\Sigma_{A_\lambda}^{\text{DC}})_{ij}\right]\delta_{(ij)\in A_\lambda}, \quad (4)$$

where $(\Sigma^{\text{weak}})^\mathbf{k}$ denotes the perturbatively evaluated weak correlation solution of the entire system, $(\Sigma_{A_\lambda}^{\text{non-pert}})$ the non-perturbatively evaluated contribution within the orbital set A_λ, $\lambda = 1, ..., M$, and the double-counting term $(\Sigma_{A_\lambda}^{\text{DC}})$ ensures that no self-energy contribution is counted twice. $\delta_{(ij)\in A_\lambda}$ is 1 only if both orbital i and orbital j are part of subspace A_λ, and 0 otherwise.

The corresponding interacting Green's function is

$$(G^{\text{SEET}}(i\omega_n))^\mathbf{k} = \left[(i\omega_n + \mu) - h^{0,\mathbf{k}} - (\Sigma^{\text{SEET}}(i\omega_n))^\mathbf{k}\right]^{-1}. \quad (5)$$

In this work, $(\Sigma^{\text{weak}})^\mathbf{k}$ is evaluated as the GW self-energy with the interacting propagator $(G^{\text{SEET}})^\mathbf{k}$ of the system, $\mathcal{F}_{GW}[(G^{\text{SEET}})^\mathbf{k}]$. Similarly, $\Sigma_{A_\lambda}^{\text{DC}}$ is evaluated as the GW self-energy with its vertices restricted to orbital subset A_λ.

Choosing the subspace of correlated orbitals local to each unit cell implies that Fourier transforming Eq. 4 to real space yields

$$(\Sigma^{\text{SEET}})_{ij}^{\mathbf{R}\mathbf{R}'} = (\Sigma^{\text{weak}})_{ij}^{\mathbf{R}\mathbf{R}'}$$
$$+ \sum_{\lambda=1}^M \left[(\Sigma_{A_\lambda}^{\text{non-pert}})_{ij} - (\Sigma_{A_\lambda}^{\text{DC}})_{ij}\right]\delta_{(ij)\in A_\lambda}\delta_{\mathbf{R}\mathbf{R}'} \quad (6)$$

where $\mathbf{R}$ and $\mathbf{R}'$ are unit cell indices.

The Dyson equation then defines the inverse Green's function in orbital space A_λ,

$$(G^{\text{SEET},-1})_{ij\in A_\lambda}^{\mathbf{R}\mathbf{R}} = \left[(i\omega_n + \mu)\mathbf{1} - h_{ij\in A_\lambda}^{0,\mathbf{R}\mathbf{R}} - (\Sigma^{\text{SEET}})_{ij\in A_\lambda}^{\mathbf{R}\mathbf{R}}\right]. \quad (7)$$

We emphasize that $(G^{\text{SEET},-1})_{ij\in A_\lambda}^{\mathbf{R}\mathbf{R}} \neq [(G^{\text{SEET}})_{ij\in A_\lambda}^{\mathbf{R}\mathbf{R}}]^{-1}$, i.e. the inverse Green's function restricted to subset A_λ is not equal to the inverse of the Green's function restricted to A_λ.

The difference between those two quantities,

$$
\begin{aligned}
&\left[(G^{\text{SEET}})^{\mathbf{RR}}_{ij\in A_\lambda}\right]^{-1} \\
&= \left[(i\omega_n + \mu)\mathbf{1} - h^{0,\mathbf{RR}}_{ij\in A_\lambda} - (\Sigma^{\text{SEET}})^{\mathbf{RR}}_{ij\in A_\lambda}(i\omega_n) - \Delta^{A_\lambda}_{ij\in A_\lambda}(i\omega_n)\right],
\end{aligned}
\tag{8}
$$

defines the hybridization function $\Delta^{A_\lambda}_{ij}$.

B. Impurity Hamiltonian construction

By splitting the static and dynamic part of each self-energy contribution ($\Sigma(i\omega_n) = \Sigma_\infty + \Sigma_{\text{corr}}(i\omega_n)$), we can reorder terms in Eq. 5 such that

$$
\begin{aligned}
\left[(G^{\text{SEET}})^{\mathbf{RR}}_{ij\in A_\lambda}\right]^{-1} &= \left[(i\omega_n + \mu)\mathbf{1} - \tilde{h}^{0,\mathbf{RR}}_{ij\in A_\lambda} - \Sigma^{\text{corr},\mathbf{RR}}_{ij\in A_\lambda}(i\omega_n)\right. \\
&\left. - \Sigma^{\text{non-pert}}_{ij\in A_\lambda}(i\omega_n) - \Delta^{A_\lambda}_{ij\in A_\lambda}(i\omega_n)\right],
\end{aligned}
\tag{9}
$$

where $\tilde{h}^{0,\mathbf{RR}}_{ij\in A_\lambda} = h^{0,\mathbf{RR}}_{ij\in A_\lambda} + (\Sigma^{\text{weak}}_\infty)^{\mathbf{RR}}_{ij\in A_\lambda} - (\Sigma^{\text{DC}}_{A_\lambda,\infty})_{ij\in A_\lambda}$ is the frequency-independent renormalized non-interacting Hamiltonian and $\Sigma^{\text{corr},\mathbf{RR}}_{ij\in A_\lambda} = (\Sigma^{\text{weak}}_{\text{corr}})^{\mathbf{RR}}_{ij\in A_\lambda} - (\Sigma^{\text{DC}}_{A_\lambda,\text{corr}})_{ij\in A_\lambda}$ is the local dynamic self-energy without double counting contribution. In order to solve $\Sigma^{\text{non-pert}}_{A_\lambda}$, we define the auxiliary propagator

$$
g^{-1}_{A_\lambda} = g^{0,-1}_{A_\lambda} - \Sigma^{\text{non-pert}}_{ij\in A_\lambda},
\tag{10}
$$

where the inverse of the non-interacting auxiliary counterpart $g^{0,-1}_{A_\lambda}$ is defined as

$$
g^{0,-1}_{A_\lambda} = (i\omega_n + \mu)\mathbf{1} - \tilde{h}^{0,\mathbf{RR}}_{ij\in A_\lambda} - \Delta^{A_\lambda}_{ij\in A_\lambda}.
\tag{11}
$$

The Green's function of Eq. 10 can then be obtained by solving an auxiliary quantum impurity problem [33]

$$
\begin{aligned}
H^{A_\lambda}_{\text{imp}} &= \sum_{ij\in A_\lambda,\sigma}(\tilde{h}^0_{ij\sigma} - \mu\delta_{ij})c^\dagger_{i\sigma}c_{j\sigma} + \sum_{b,\sigma}\epsilon_{b\sigma}a^\dagger_{b\sigma}a_{b\sigma} \\
&+ \sum_{i\in A_\lambda,b,\sigma}(V_{ib\sigma}c^\dagger_{i\sigma}a_{b\sigma} + h.c.) + \frac{1}{2}\sum_{\substack{ijkl\in A_\lambda \\ \sigma\sigma'}}v_{ijkl}c^\dagger_{i\sigma}c^\dagger_{k\sigma'}c_{l\sigma'}c_{j\sigma}
\end{aligned}
\tag{12}
$$

within the subset A_λ where $a^\dagger_{b\sigma}$ ($a_{b\sigma}$) are creation (annihilation) operators for bath orbital b with spin σ. The energy levels $\{\epsilon_{b\sigma}\}$ and couplings between bath (b) and impurity orbitals (i) $V_{ib\sigma}$ can be approximated by discretizing the continuous hybridization function with a finite number N_b of bath orbitals

$$
\Delta^{A_\lambda}_{ij\sigma}(i\omega_n) = \sum_{b=1}^{N_b}\frac{V_{ib\sigma}V_{jb\sigma}}{i\omega_n - \epsilon_{b\sigma}}.
\tag{13}
$$

The expressions for Σ (as a function of G) and G (as a function of Σ) lead to self-consistent equations that are
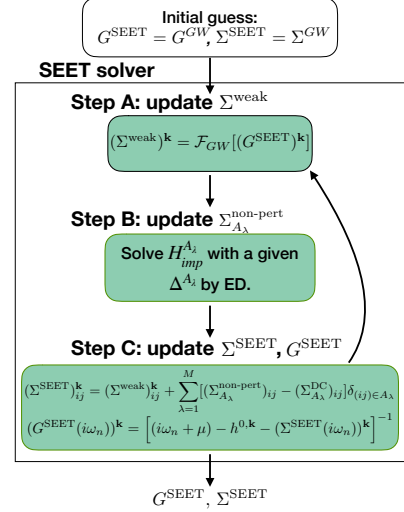
Figure 1. Workflow of self-consistent SEET. $H^{A_\lambda}_{\text{imp}}$ and Δ^{A_λ} are defined in Eq. 12 and 8.

Φ-derivable and therefore conserving and thermodynamically consistent [23]. We emphasize that the two-body Coulomb interactions remain the bare interactions of the original electronic Hamiltonian (Eq. 1). Screening effects are addressed by the explicit treatment of $\Sigma^{\text{corr},\mathbf{RR}}_{ij\in A}$ in Eq. 9, and contain all screening contributions on the level of the weak correlation method, as well as non-perturbative correlation effects due to correlations in the subspace A_λ. The method is different from DMFT and other embedding methods where the self-consistency condition is different, the local self-energy contains no contributions from the weak coupling terms, and interaction parameters are typically treated as free parameters in the early LDA+DMFT formulations [34].

The SEET equations are solved iteratively until convergence in all quantities is achieved [35]. The self-consistency loop is illustrated in Fig. 1. At step A, a single iteration of GW, $\mathcal{F}_{GW}[(G^{\text{SEET}})^{\mathbf{k}}]$, is executed to update $(\Sigma^{\text{weak}})^{\mathbf{k}}$ for the whole system. Along with the definition of hybridization function Δ^A in Eq. 8, step B corresponds to solving $H^{A_\lambda}_{\text{imp}}$ with a quantum impurity solver. When multiple subspaces A_λ are defined, $H^{A_\lambda}_{\text{imp}}$ for each subset is solved independently. Lastly, Σ^{SEET} and G^{SEET} are updated according to Eq. 4 and 5 with the new Σ^{weak} and $\Sigma^{\text{non-pert}}_{A_\lambda}$.

Note that the SEET framework can be adapted to use other diagrammatic many-body perturbation approximations as the weakly correlated method, as long as the double counting correction can be rigorously defined. For additional discussion of the method see Ref. [23].

III. COMPUTATIONAL DETAILS

We solve the electronic structure Hamiltonian Eq. 1 in a Gaussian *gth-dzvp-molopt-sr* basis [36] with *gth-*

pbe pseudopotential [37] and decompose the four-fermion Coulomb integrals into a combination of auxiliary even-tempered Gaussians for Sr and *def2-svp-ri* [38] bases for all other atoms, using up to $6 \times 6 \times 6$ k-points in the Brillouin zone. Integrals are obtained with the open source PySCF [39] package.

All dynamic quantities in SEET are computed on the imaginary time and frequency axis. Efficient representations for both imaginary time and frequency grids are essential for realistic material calculations. In this work, we use the compact intermediate representation (IR) [40] with sparse frequency sampling [41] for all dynamical quantities such as Green's function and self-energy. In IR, the grid size is governed by a dimensionless parameter Λ that should be at least larger than $\beta \omega_{\max}$ where β is the inverse temperature and $\omega_{\max}$ is the energy bandwidth of the system. Lower temperature and larger energy bandwidth would require larger grid size and thereby increase computational linear with β. Simulations are performed at temperature $T \sim 1579K$ ($\beta = 200$ Ha^{-1}) for SrVO$_3$ and 1053 K ($\beta = 300$ Ha^{-1}) for SrMnO$_3$.

We choose the strongly correlated subspace to be the local transition metal $3d$ orbitals (split into t_{2g} and e_g) as well as the oxygen p orbitals. Note that standard DMFT impurity constructions typically include t_{2g} [1–8, 11–13, 15, 17] or $t_{2g} + e_g$ [12, 13, 17] orbitals, though methods to treat entire unit cells have recently been pioneered [42]. In order to gradually improve our solution, we examine the effect of also treating the correlations on the oxygen p orbitals exactly. In order to make impurity size feasible for ED calculations, we further split the O $2p$ shell into two $2p_\pi$ and one $2p_\sigma$ orbitals, defined with respect to the transition metal ion.

IV. STRONTIUM VANADATE

Name	Imp	Description
A	1	V t_{2g}
B	3	V t_{2g}; O p_π; O p_σ
C	4	V t_{2g}; V e_g; O p_π; O p_σ

Table I. Choice of the impurities for SrVO$_3$. Imp denotes the number of distinct disjoint impurity problems.

SrVO$_3$ is a simple correlated metal with an undistorted cubic perovskite structure. Nominally, it has a single electron in the vanadium d-shell. Photoemission spectroscopy (PES) and bremsstrahlung isochromat spectroscopy (BIS) show a pronounced renormalized quasiparticle peak at the Fermi level (E_F), a weak satellite peak at ~ -1.8 eV, and a strong satellite peak at ~ 3 eV [2, 43, 44]. V $2p - 3d$ resonance photoemission further attributes V $3d$ character both to the quasiparticle peak at E_F and to the lower satellite feature at around

-1.8 eV [2, 43]. Features between -3 eV and -10 eV are mainly attributed to the O p states [2, 43–45].

In Fig. 2, for SrVO$_3$, we show a calculated local single particle spectral function $A(\omega)$ as a function of frequency ω.

This spectral function was analytically continued [46, 47] from the imaginary to the real axis and it was orbitally resolved to display V t_{2g}(blue), V e_g(orange) and O $2p$ and $3p$ orbitals. Contributions from all other orbitals are included as "rest". The experimental results for PES (Ref. [43]) and for BIS (Ref. [44]) are also plotted for easy comparison.

scGW results show a clear $p - d$ splitting. Quasiparticle peaks around E_F are dominated by V t_{2g} while the density of state (DOS) between -2.5 and -10 eV is dominated by O p orbitals with the first and second peak mainly corresponding to O p_π and O p_σ. The conduction band peak around 3 eV is interpreted as V e_g orbitals, rather than an upper Hubbard band from t_{2g} orbitals. Except for the missing lower satellite peak around ~ -1.8 eV, scGW results qualitatively agree with photoemission spectroscopy. In contrast to the experimental quasiparticle peak at E_F, scGW has a much wider feature (note that the k-space discretization artificially introduces a double peak structure), consistent with a spectrum calculated with non-local GW self-energy in Ref. [48]. In addition, the O p peaks are shifted upward from -3 eV to -4 eV [45].

Next, we discuss the self-consistent SEET embedding construction with local V t_{2g} states included non-perturbatively in an impurity (SEET, setup A). In contrast to scGW in SEET with setup A, the width of the t_{2g} near-Fermi-energy peak is reduced to 1.5 eV which is much closer to experimental data. The oxygen p states are shifted upward in energy and there is a large gap between unoccupied t_{2g} and e_g states. However, the oxygen shift is inconsistent with PES and the $t_{2g} - e_g$ splitting is inconsistent with BIS.

SEET with setup B adds strong correlations to oxygen $2p$ orbitals in addition to the V t_{2g}. Since the three oxygen atoms in the unit cell are identical, we only consider the $2p$ orbitals from one oxygen atom. Non-perturbative corrections to the other two oxygen atoms are included by symmetry. We observe a shift of the oxygen p states back to lower energies but little change for other orbitals.

Adding correlation from V e_g orbitals in SEET with setup C moves the e_g conduction bands towards lower energy leading to a spectrum consistent with BIS data. In this setup the oxygen p states are shifted to the location found in PES, recovering the pronounced $p - d$ splitting. However, the so called lowered satellite photoemission peak at -1 to -2 eV is not recovered. The lack of this peak in SEET may be due to several reasons. First, the Gaussian basis set employed may not contain a good description of orbitals necessary to evaluate this peak. However, we find this possibility unlikely since SEET calculations performed in a larger basis set still cannot recover this lower satellite peak. (For details see
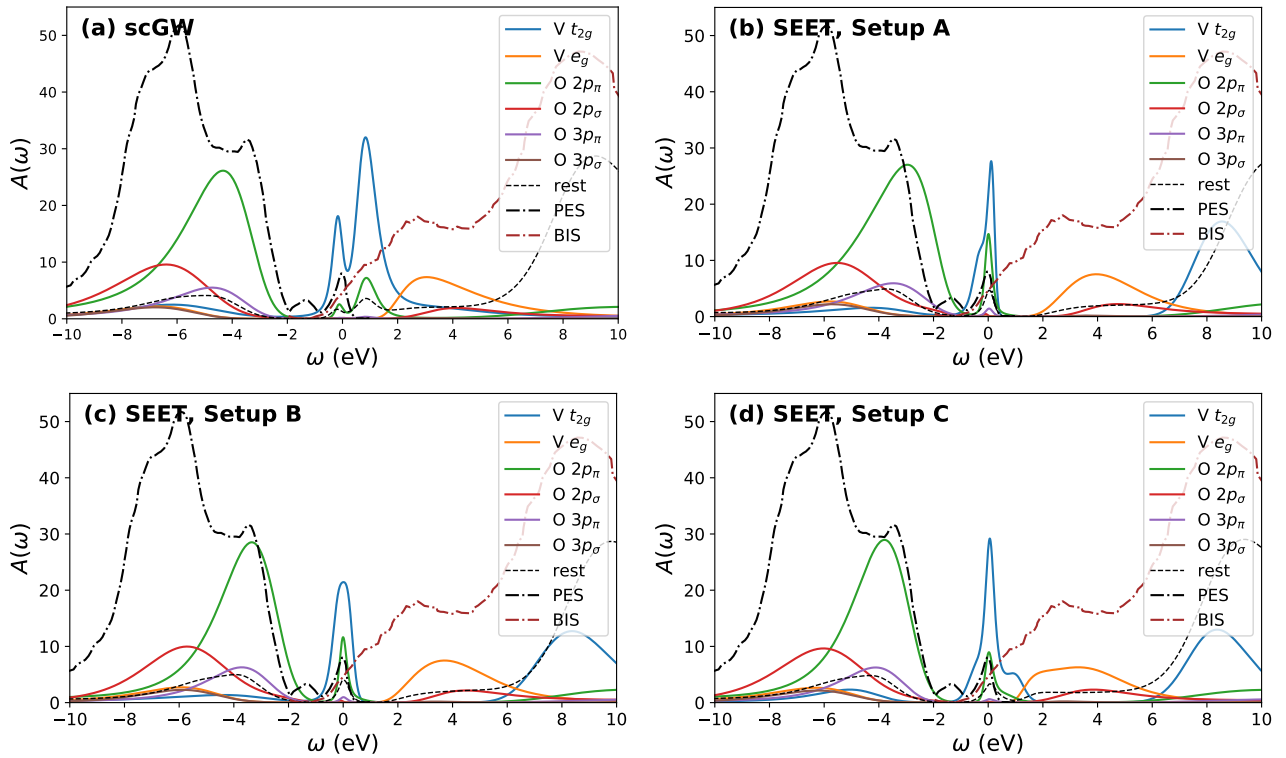
Figure 2. Local orbital-resolved DOS of SrVO$_3$ from scGW and SEET. Impurity choices are shown in Table I. The PES and BIS data are obtained from Ref. [43, 44]. The experimental data are rescaled to match results from analytical continuation.

appendix). Second, correlations beyond GW that have not been considered here such as strong correlations in higher orbitals (e.g. $4d$) or cross-correlations between disjoint impurities (such as $p - d$ correlations) may be responsible for arising of this peak. These correlations beyond GW could be added to SEET if a larger impurity combing $p - d$ orbitals or containing $4d$ orbitals would be considered. Lastly, this lower satellite peak may be caused by an insufficiency of the GW description for multiple orbitals that cannot be simply contained in SEET as multiple larger impurity problems. This lower satellite peak is observed in multitier GW+EDMFT calculations performed in Ref. [17] that attributes it to non-local Coulomb interaction.

The total local DOS for SrVO$_3$ is shown in Fig. 3. As we systematically add correlations, SEET reaches quantitatively better agreement with the experimental data. The quasiparticle peak around E_F is dominated by V t_{2g} while the DOS between -2.5 and -10 eV is dominated by O p orbitals, with the first and second peak mainly corresponding to O p_π and O p_σ. In the conduction bands, the shoulder at ≈ 1 eV and the peak at $\sim 2.5-3$ eV are assigned to V $t_{2g} + e_g$ and V e_g respectively while the peak at ≈ 8 eV is dominated by Sr $4d$ orbitals. The fact that scGW predicts a better $p - d$ splitting compared to SEET with setup A implies that there may be error cancellation to the missing local t_{2g} correlation beyond GW. In general, it is difficult to precisely determine the
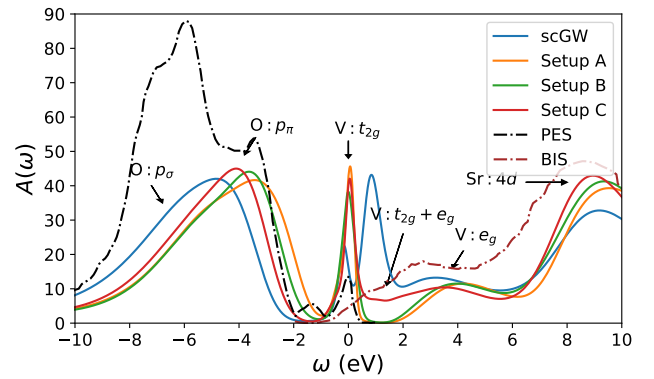

Figure 3. Total local density of states of SrVO$_3$ from scGW and SEET with different impurity choices. Arrows indicate the orbital contributions according to SEET with impurity choice C. The PES and BIS data is obtained from Ref. [43, 44]

source of this cancelation since it could be non-local correlations beyond GW from any orbital (e.g. O p) or local correlations beyond GW from orbitals other than V t_{2g}. However, as shown in Fig. 2 and 3, the position of the O p bands gradually reaches better agreement with experiment from SEET with setup B and C as local self-energy correction of O $2p$ and V e_g are added. We believe the error cancellation between strong local correlation from V $3d$ and O $2p$ are the reason that scGW outperforms

SEET with setup A.

In Fig. 4, we show the SEET (setup C) V t_{2g} local self-energy, analytically continued from the imaginary to the real frequency axis. The strong pole at around 3.5 eV is consistent with the absence of a V t_{2g} upper Hubbard band at around 3.0 eV, and shifts additional V t_{2g} features near 8 eV. The quasiparticle renormalization factor Z can be computed through $Z^{-1} = [1 - \partial \mathrm{Re}\Sigma(\omega)/\partial\omega\big|_{\omega=0}]$ for scGW ($Z = 0.7$) and SEET with impurity setup C ($Z = 0.27$). In the presence of local self-energy corrections to the V t_{2g} orbitals, the V t_{2g} quasiparticle peak has been strongly renormalized. The reduction of Z from 0.7 to 0.27 is smaller than the experimental value of $Z = 0.5 \sim 0.6$ [2, 49] and data from other theoretical calculations [2, 4–6]. Note that our Z is similar to that of LDA+DMFT (see the inset of Fig. 5 in Ref. [5]) if the self-energy derivative is taken over the same interval.
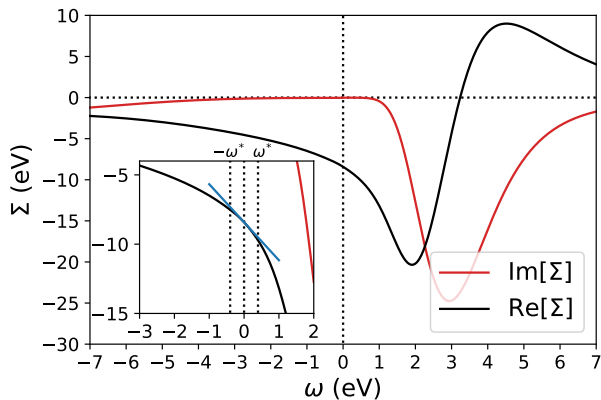

Figure 4. V t_{2g} local self-energy from SEET with impurity setup C, analytically continued to the real frequency axis. The estimated quasiparticle regime is around $[-\omega^*, \omega^*]$ where $\omega^* = 0.4$ eV.

Typical failures of LDA for SrVO$_3$ include (i) a t_{2g} quasiparticle bandwidth that is too large, (ii) missing lower/upper satellite peaks, and (iii) an incorrect position of orbitals outside the V $3d$ shell [1–6].

In the LDA+DMFT scheme, the Coulomb interaction U and the Hund's coupling J are usually chosen *ad hoc* such that a lower/upper Hubbard band emerges [1, 3, 12]. Sometimes J determined from Hartree-Fock calculations on model Hamiltonians [50] is chosen. A double counting shift of the chemical potential is chosen such that the number of electrons in the DMFT is fixed ($3d^1$ configuration in this case), assuming that the strongly correlated subspace is well separated from all other orbitals. With these parameters, LDA+DMFT produces a quasiparticle band narrowing and a broad satellite at around -1.8 eV [1, 3]. Less *ad hoc* parameter choices have also been considered but result in less accurate results. For example, U and J determined by constrained LDA (cLDA) [14] place the lower Hubbard band too low in energy (between -2.0 to -2.3 eV) [2, 4–6] and the FLL double

counting [51] results in an incorrect $p-d$ splitting in the occupied bands [9, 10]. In LDA+DMFT, the lower satellite is interpreted as a Hubbard band due to strong local correlations on the vanadium atoms.

In addition to LDA+DMFT, variants of G_0W_0+DMFT have been applied to SrVO$_3$ [6–8, 11]. In this scheme, $U(\omega)$ and $J(\omega)$ are determined through constrained RPA (cRPA) [18] based on G_0W_0 and the double counting correction has a rigorous definition if self-consistency is achieved, unlike in LDA+DMFT. In general, G_0W_0+DMFT predicts qualitatively similar results to LDA+DMFT except for the wider t_{2g} quasiparticle bandwidth [8] and better agreement of the lower satellite feature with photoemission data [6]. As in LDA+DMFT, the lower satellite peak is caused by Hubbard physics.

Recent studies from multitier GW+EDMFT found screening beyond GW in the V t_{2g} orbitals. These effects are resulted from (i) retarded on-site interactions in EDMFT and (ii) local vertex corrections to the polarization [15–17]. Note that during the self-consistency loop of multitier GW+EDMFT, local vertex corrections to the polarization are involved in the evaluation of the non-local screened interaction. The resulting renormalized screened interaction therefore contains more non-local correlations than the one from GW. These results attribute the lower satellite feature to a non-local plasmon, rather than Hubbard physics. This interpretation is also consistent with the findings from the cumulant expansion based on quasiparticle GW [52].

Although cross-correlations or contributions from higher states, as well as the non-local plasmonic physics examined in multitier GW+EDMFT, are outside the physics investigated here, our calculations offer additional insight into the origin of the lower satellite peak at around -1.8 eV. While Ref. [15–17] include only V t_{2g} and e_g orbitals in the correlated subspace, we find that O $2p$ orbitals do not contribute to this peak. Instead, the strong local correlations from O $2p$ improve the the $p-d$ splitting in the presence of non-perturbative V t_{2g} local correlations.

A second observation concerns the contribution of the experimentally observed incoherent feature around 3.0 eV [44] that is traditionally attributed to the upper Hubbard band of the t_{2g} orbitals and e_g orbitals. In our calculation, this peak has only e_g character, consistent with some of the literature [7, 11, 52].

V. STRONTIUM MANGANATE

SrMnO$_3$ is a cubic insulating perovskite with nominal filling of three electrons in the Mn $3d$ shell. Its magnetism is experimentally observed as G-type antiferromagnetic (AFM) ordering at low temperature and PM ordering at high temperature (with Néel temperature $T_N \sim 233-260$ K) [54, 55]. The paramagnetic state has been studied in photoemission [53, 56–58] and gap values ranging from
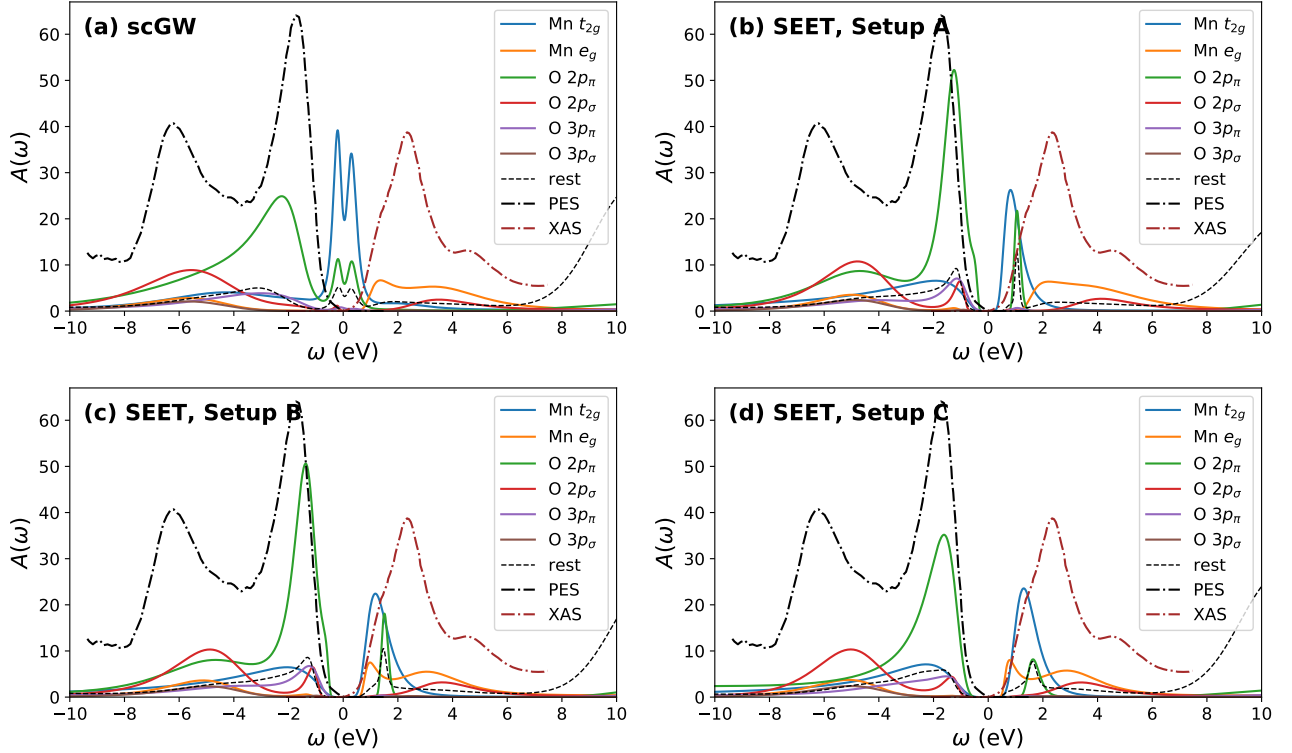
Figure 5. Local orbital-resolved DOS of SrMnO$_3$ from scGW and SEET. The impurity choices correspond to (A), (B), and (C) in Table II. Dotted lines are PES and soft x-ray absorption spectroscopy (XAS) from Ref. [53].

Name	Imp	Description
A	1	Mn t_{2g}
B	2	Mn t_{2g}; Mn e_g
C	4	Mn t_{2g}; Mn e_g; O p_π; O p_σ

Table II. Choice of the impurities for SrMnO$_3$. Imp denotes the number of distinct disjoint impurity problems.

$1.0-2.3$ eV have been found. To our knowledge, a detailed experimental analysis of the orbital character of the near-Fermi-surface states has not been performed. Theoretical calculations so far are limited to the AFM state [9, 17, 59].

Fig. 5 shows the total local orbital-resolved DOS from scGW and SEET with different impurity choices in the PM phase at 1053 K (see Table. II). In GW, SrMnO$_3$ is incorrectly predicted to be metallic. The corresponding spectral functions are similar to SrVO$_3$, where bands around E_F are dominated by transition metal t_{2g} states. However, hybridizations between Mn $3d$ and O $2p$ are much stronger, pushing the O $2p$ bands closer to E_F. This strong hybridization puts the validity of impurity models with only Mn $3d$ orbitals in doubt. The qualitative failure of scGW implies the need of self-energy diagrams beyond GW approximation.

We first include local self-energy corrections within only the Mn t_{2g} orbitals as shown in Setup A of Fig. 5. The non-perturbative treatment of Mn t_{2g} greatly suppress the DOS at E_F and opens the gap for SrMnO$_3$ which is formed by Mn t_{2g} + O p_π hybridized orbitals both above and below the gap. However, the gap is substantially smaller than the one found in photoemission data [53].

Next, we include Mn e_g orbitals in setup B. The non-perturbative treatment of the Mn e_g orbitals results in the conduction band peak of the e_g orbitals being pushed below the t_{2g} peak and the gap edge aligning. Most of the higher valence band states have O $2p_\pi$ character, while most of the lower conduction band states have Mn t_{2g} and Mn e_g character.

Finally, we include O $2p$ orbitals in impurity setup C. Similar to SrVO$_3$, only the $2p$ orbitals from one oxygen atom are considered. Local self-energy correction beyond GW from O $2p$ further push both Mn t_{2g} and O p_π away from E_F. Besides that, there is little change to the remaining orbitals.

SEET successfully opens a gap for all impurity choices shown in Fig. 6. Note that this gap is opened due to the full self-consistency between high and low levels loops in SEET. It only opens when GW orbitals are updated at every iteration to include strong correlation effects that arise from the solution of the impurity problems. We illustrate the opening of the gap versus iteration number as well as the exact convergence for electronic energies
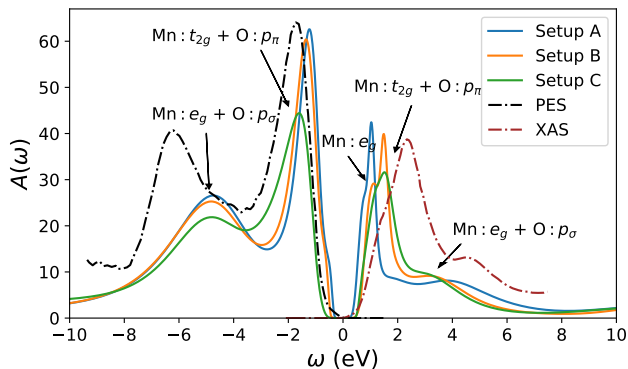
Figure 6. Sum of Mn $3d$ + O $2p$ local DOS from SEET with different impurity choices. Dotted lines are photoemission data from Ref. [53].

in the appending. Systematic enlarging of the number of impurities leads to a convergence to the experimental data. The first and second valence peaks at -2.0 and -6.5 eV correspond to Mn t_{2g} + O p_π and Mn e_g + O p_σ. In the conduction band, the shoulder at 1 eV corresponds to Mn e_g bands, and the two peaks at -2.5 and -4.8 eV corresponds to Mn t_{2g} + O p_π and Mn e_g + O p_σ. The gap is formed by Mn t_{2g} + O p_π valence band and Mn e_g conduction bands.

The agreement with PES and XAS is not perfect. While such a difference may arise due to the finite size effects present, we eliminated this possibility by caring out calculations for different numbers of k-points. For details see appendix. Since finite size effects are negligible, the differences are likely due to either (i) inter-orbital correlations between different independent impurities, and/or (ii) non-local correlations outside of GW, (iii) employed Gaussian basis set.

Fig. 7 shows the k-resolved partial DOS along $R - \Gamma - X$. The hybridization between Mn t_{2g} and O p_π is clearly visible in the k-resolved partial DOS. The indirect gap is formed between Mn t_{2g}+ O p_π valence states at R and Mn e_g conduction band states at the Γ point, which is consistent with our conclusion from the local DOS in Fig. 5 and 6.

Several previous works have studied the electronic structure of the low-temperature AFM SrMnO$_3$ using density functional theory (DFT) [53, 59], and variants of GW [17, 60], LDA+DMFT [61] and GW+DMFT [17]. On the other hand, understanding of the high-temperature PM phase is limited. LDA incorrectly predicts a metallic phase for PM SrMnO$_3$ [9, 10, 13], suggesting that a mean-field description is insufficient. Furthermore, G_0W_0 on top of DFT also fails to open a gap [17]. To address the missing correlations, LDA+DMFT can be applied, assuming that strong correlations are purely local on the Mn atom [9, 10, 13]. In that case, both the U and J model parameters need to be chosen *ad hoc* in order to reproduce experimental data, and the double counting has to be fine-tuned to keep the

system insulating. The failure of standard FLL double counting likely comes from the strong hybridization between Mn $3d$ and O $2p$. The band gap, as well as the type of insulating state (e.g. Mott or charge-transfer), are highly sensitive to the parameter choice.

Petocchi *et al.* [17] applied multitier GW+EDMFT to both the PM and AFM phase. Even though a gap opening for AFM is observed, a strongly correlated metal in proximity to a Mott transition is observed in PM phase. This is likely due to the lack of outer-loop self-consistency for the entire system. Such an outer loop is responsible for updating all the weakly correlated orbitals to include strong correlation effects coming form the solution of the impurity problem. In order to verify this, we have performed SEET calculations without the outer-loop self-consistency for all impurity choices. We observe that even though the non-perturbative treatments of the impurities greatly suppresses the DOS at E_F, the lack of outer-loop self-consistency results in an incorrect chemical potential shift so that a non-zero DOS is observed (see Fig. 12 in appendix E). Note that a similar non-zero DOS is observed in Ref. [17]. The metallic character observed in Ref. [17] may also arise due the missing correlations beyond GW from O $2p$ or a failure of cRPA to produce correct screened interactions.

VI. CONCLUSIONS

We have analyzed single-particle spectral functions of two paradigmatic strongly correlated cubic perovskites. Our starting point was the description of the solid in a Bloch-wave basis consisting of Gaussian orbitals, which allows for a clear attribution of correlation physics to individual atomic orbitals. By analyzing strong correlations in multiple choices of impurity orbitals, we showed that the usual procedure of isolating 3-5 local orbitals near the Fermi energy is insufficient to describe the physics of these systems if ab-initio Coulomb interactions are used. We have also illustrated that an interpretation in terms of 'Hund's physics' with empirically adjusted interaction parameters of low-lying bands is not necessary. Rather, by systematically adding non-perturbative correlations, also to orbitals not immediately adjacent to the Fermi energy, we could show a gradual convergence of most aspects of the spectral function to the experimental result.

In the case of SrVO$_3$, we presented that the standard DMFT interpretation of the material as a correlated 3-orbital 'Hunds' metal with a three-peak structure of lower and upper Hubbard side-peaks, as well as a central quasi-particle peak, is not consistent with our formulation. Through the explicit inclusion of O $2p$ impurities, we also showed that O $2p$ orbitals do not contribute to the lower/upper incoherent feature at around -1.8/3.0 eV. The absence of the lower satellite from our calculations indicates that additional physics arising either from non-local processes, higher bands, or/and inter-orbital cross-
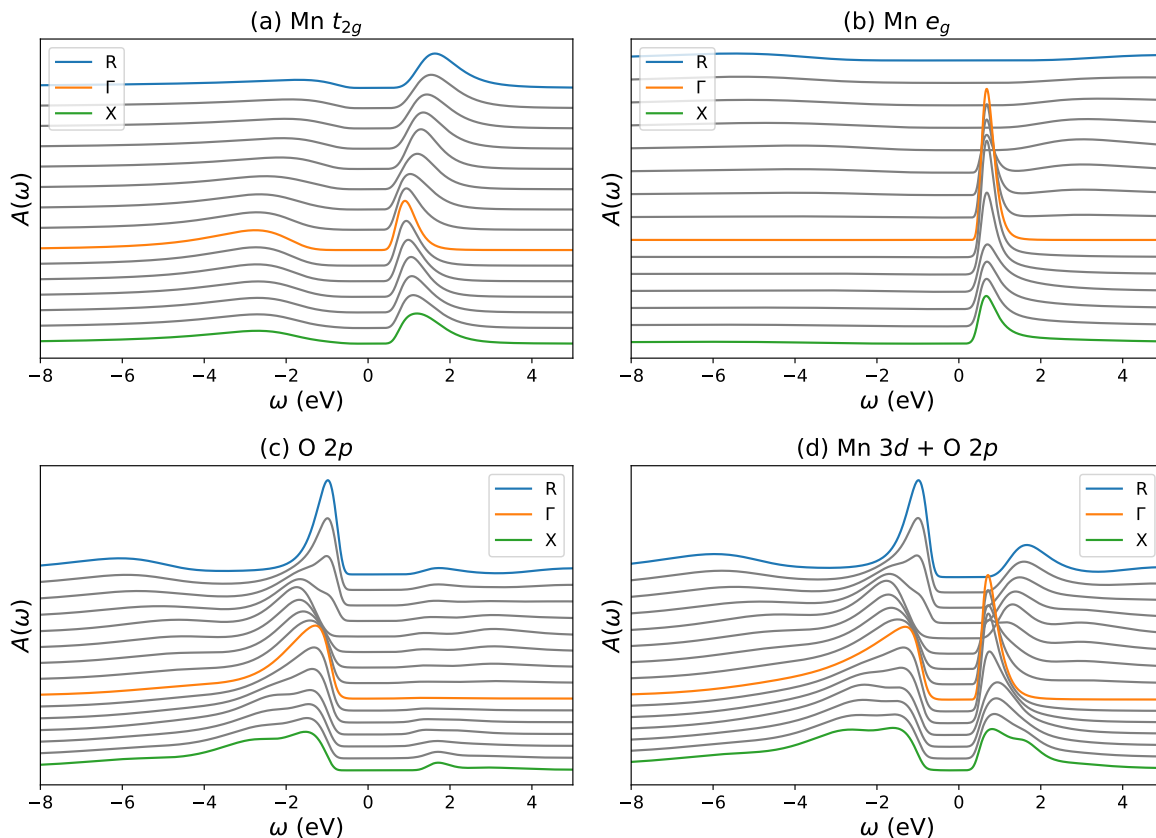
Figure 7. Momentum and orbital-resolved partial density of states $A(\omega)$ as a function of frequency ω of SrMnO$_3$ from SEET with impurity setup C. Shown are Mn t_{2g}, Mn e_g, O p, and combined contributions along a high-symmetry path in the BZ from R to Γ to X.

correlations is important. In the case of SrMnO$_3$, we illustrated the importance of the feedback of the strongly correlated self-energy to the remainder of weakly correlated orbitals present in the system, leading successfully to an insulating behavior in PM phase.

In contrast to other methods commonly in use, the procedures employed in this paper are uniquely defined in terms of Gaussian basis sets, choice of correlated orbitals, and choice of correlated subspaces, making every step of the calculation independently reproducible.

Our work illustrates that the SEET procedure is able to recover correct results in strongly-correlated realistic systems, and that systematic addition of correlations in orbital subgroups leads to a systematic understanding of single-particle excitation spectra.

VII. ACKNOWLEDGEMENT

[1] E. Pavarini, S. Biermann, A. Poteryaev, A. I. Lichtenstein, A. Georges, and O. K. Andersen, Phys. Rev. Lett. **92**, 176403 (2004).

[2] A. Sekiyama, H. Fujiwara, S. Imada, S. Suga, H. Eisaki, S. I. Uchida, K. Takegahara, H. Harima, Y. Saitoh, I. A. Nekrasov, G. Keller, D. E. Kondakov, A. V. Kozhevnikov, T. Pruschke, K. Held, D. Vollhardt, and V. I. Anisimov, Phys. Rev. Lett. **93**, 156402 (2004).

[3] F. Lechermann, A. Georges, A. Poteryaev, S. Biermann, M. Posternak, A. Yamasaki, and O. K. Andersen, Phys. Rev. B **74**, 125120 (2006).

[4] I. A. Nekrasov, G. Keller, D. E. Kondakov, A. V. Kozhevnikov, T. Pruschke, K. Held, D. Vollhardt, and V. I. Anisimov, Phys. Rev. B **72**, 155106 (2005).

[5] I. A. Nekrasov, K. Held, G. Keller, D. E. Kondakov, T. Pruschke, M. Kollar, O. K. Andersen, V. I. Anisimov, and D. Vollhardt, Phys. Rev. B **73**, 155112 (2006).

[6] C. Taranto, M. Kaltak, N. Parragh, G. Sangiovanni, G. Kresse, A. Toschi, and K. Held, Phys. Rev. B **88**, 165119 (2013).

[7] J. M. Tomczak, M. Casula, T. Miyake, F. Aryasetiawan, and S. Biermann, EPL (Europhysics Letters) **100**, 67001 (2012).

[8] R. Sakuma, P. Werner, and F. Aryasetiawan, Phys. Rev. B **88**, 235110 (2013).

[9] H. T. Dang, X. Ai, A. J. Millis, and C. A. Marianetti, Phys. Rev. B **90**, 125114 (2014).

[10] H. Chen, H. Park, A. J. Millis, and C. A. Marianetti, Phys. Rev. B **90**, 245138 (2014).

[11] J. M. Tomczak, M. Casula, T. Miyake, and S. Biermann, Phys. Rev. B **90**, 165138 (2014).

[12] D. Bauernfeind, M. Zingl, R. Triebl, M. Aichhorn, and H. G. Evertz, Phys. Rev. X **7**, 031013 (2017).

[13] D. Bauernfeind, R. Triebl, M. Zingl, M. Aichhorn, and H. G. Evertz, Phys. Rev. B **97**, 115156 (2018).

[14] O. Gunnarsson, O. K. Andersen, O. Jepsen, and J. Zaanen, Phys. Rev. B **39**, 1708 (1989).

[15] L. Boehnke, F. Nilsson, F. Aryasetiawan, and P. Werner, Phys. Rev. B **94**, 201106 (2016).

[16] F. Nilsson, L. Boehnke, P. Werner, and F. Aryasetiawan, Phys. Rev. Materials **1**, 043803 (2017).

[17] F. Petocchi, F. Nilsson, F. Aryasetiawan, and P. Werner, Phys. Rev. Research **2**, 013191 (2020).

[18] F. Aryasetiawan, M. Imada, A. Georges, G. Kotliar, S. Biermann, and A. I. Lichtenstein, Phys. Rev. B **70**, 195104 (2004).

[19] J. M. Luttinger and J. C. Ward, Phys. Rev. **118**, 1417 (1960).

[20] G. Baym and L. P. Kadanoff, Phys. Rev. **124**, 287 (1961).

[21] G. Baym, Phys. Rev. **127**, 1391 (1962).

[22] A. A. Kananenka, E. Gull, and D. Zgid, Phys. Rev. B **91**, 121111(R) (2015).

[23] D. Zgid and E. Gull, New Journal of Physics **19**, 023047 (2017).

[24] A. A. Rusakov, S. Iskakov, L. N. Tran, and D. Zgid, Journal of Chemical Theory and Computation **15**, 229 (2019).

[25] S. Iskakov, C.-N. Yeh, E. Gull, and D. Zgid, Phys. Rev. B **102**, 085105 (2020).

[26] L. Hedin, Phys. Rev. **139**, A796 (1965).

[27] F. Aryasetiawan and O. Gunnarsson, Reports on Progress in Physics **61**, 237 (1998).

[28] A. Kutepov, S. Y. Savrasov, and G. Kotliar, Phys. Rev. B **80**, 041103 (2009).

[29] M. Caffarel and W. Krauth, Phys. Rev. Lett. **72**, 1545 (1994).

[30] S. Iskakov and M. Danilov, Computer Physics Communications **225**, 128 (2018).

[31] S. Iskakov, A. A. Rusakov, D. Zgid, and E. Gull, Phys. Rev. B **100**, 085112 (2019).

[32] P.-O. Lwdin (Academic Press, 1970) pp. 185 – 199.

[33] A. Georges, G. Kotliar, W. Krauth, and M. J. Rozenberg, Rev. Mod. Phys. **68**, 13 (1996).

[34] G. Kotliar, S. Y. Savrasov, K. Haule, V. S. Oudovenko, O. Parcollet, and C. A. Marianetti, Rev. Mod. Phys. **78**, 865 (2006).

[35] See Supplemental Material at [URL will be inserted by publisher] for selected self-consistent impurity Hamiltonians.

[36] J. VandeVondele and J. Hutter, The Journal of Chemical Physics **127**, 114105 (2007).

[37] S. Goedecker, M. Teter, and J. Hutter, Phys. Rev. B **54**, 1703 (1996).

[38] C. Httig, Phys. Chem. Chem. Phys. **7**, 59 (2005).

[39] Q. Sun, T. C. Berkelbach, N. S. Blunt, G. H. Booth, S. Guo, Z. Li, J. Liu, J. D. McClain, E. R. Sayfutyarova, S. Sharma, S. Wouters, and G. K. Chan, Pyscf: the python-based simulations of chemistry framework (2017).

[40] H. Shinaoka, J. Otsuki, M. Ohzeki, and K. Yoshimi, Phys. Rev. B **96**, 035147 (2017).

[41] J. Li, M. Wallerberger, N. Chikano, C.-N. Yeh, E. Gull, and H. Shinaoka, Phys. Rev. B **101**, 035144 (2020).

[42] T. Zhu and G. K.-L. Chan, Ab initio full cell gw+dmft for correlated materials (2020), arXiv:2003.01349 [cond-mat.str-el].

[43] K. Yoshimatsu, T. Okabe, H. Kumigashira, S. Okamoto, S. Aizaki, A. Fujimori, and M. Oshima, Phys. Rev. Lett. **104**, 147601 (2010).

[44] K. Morikawa, T. Mizokawa, K. Kobayashi, A. Fujimori, H. Eisaki, S. Uchida, F. Iga, and Y. Nishihara, Phys. Rev. B **52**, 13711 (1995).

[45] M. Takizawa, M. Minohara, H. Kumigashira, D. Toyota, M. Oshima, H. Wadati, T. Yoshida, A. Fujimori, M. Lippmaa, M. Kawasaki, H. Koinuma, G. Sordi, and M. Rozenberg, Phys. Rev. B **80**, 235104 (2009).

[46] M. Jarrell and J. Gubernatis, Physics Reports **269**, 133 (1996).

[47] R. Levy, J. LeBlanc, and E. Gull, Computer Physics Communications **215**, 149 (2017).

[48] T. Miyake, C. Martins, R. Sakuma, and F. Aryasetiawan, Phys. Rev. B **87**, 115110 (2013).

[49] T. Yoshida, K. Tanaka, H. Yagi, A. Ino, H. Eisaki, A. Fujimori, and Z.-X. Shen, Phys. Rev. Lett. **95**, 146404 (2005).

[50] T. Mizokawa and A. Fujimori, Phys. Rev. B **54**, 5368 (1996).

[51] M. T. Czyżyk and G. A. Sawatzky, Phys. Rev. B **49**, 14211 (1994).

[52] M. Gatti and M. Guzzo, Phys. Rev. B **87**, 155147 (2013).

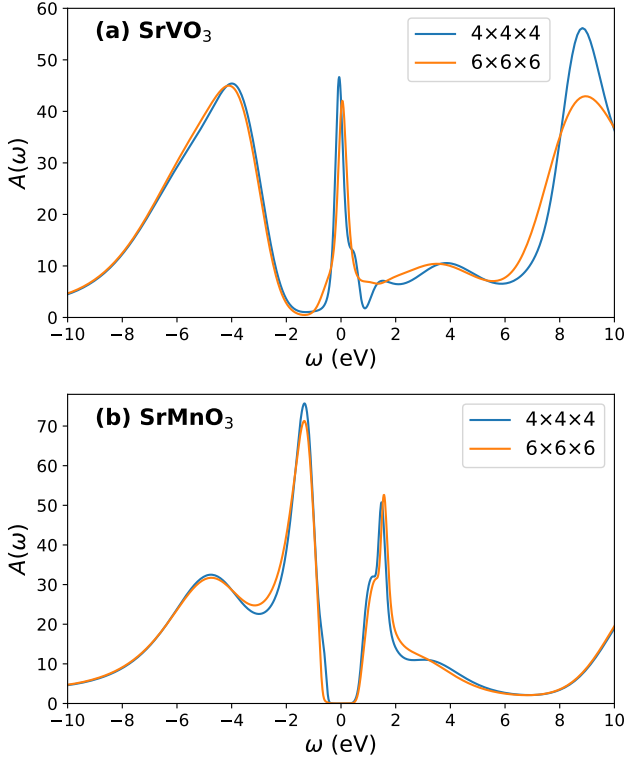[53] D. H. Kim, H. J. Lee, B. Dabrowski, S. Kolesnik, J. Lee, B. Kim, B. I. Min, and J.-S. Kang, Phys. Rev. B **81**,

Figure 8. Total local DOS for $SrVO_3$ and $SrMnO_3$ from SEET with different number of k-points in the Brillouin zone. The impurity choices are setup C in Table I for $SrVO_3$ and setup B in Table II for $SrMnO_3$.

073101 (2010).

[54] T. Negas and R. S. Roth, Journal of Solid State Chemistry **1**, 409 (1970).

[55] T. Takeda and S. hara, Journal of the Physical Society of Japan **37**, 275 (1974).

[56] M. Abbate, F. M. F. de Groot, J. C. Fuggle, A. Fujimori, O. Strebel, F. Lopez, M. Domke, G. Kaindl, G. A. Sawatzky, M. Takano, Y. Takeda, H. Eisaki, and S. Uchida, Phys. Rev. B **46**, 4511 (1992).

[57] T. Saitoh, A. E. Bocquet, T. Mizokawa, H. Namatame, A. Fujimori, M. Abbate, Y. Takeda, and M. Takano, Phys. Rev. B **51**, 13942 (1995).

[58] J.-S. Kang, H. J. Lee, G. Kim, D. H. Kim, B. Dabrowski, S. Kolesnik, H. Lee, J.-Y. Kim, and B. I. Min, Phys. Rev. B **78**, 054434 (2008).

[59] R. Søndenå, P. Ravindran, S. Stølen, T. Grande, and M. Hanfland, Phys. Rev. B **74**, 144102 (2006).

[60] Z. Ergönenc, B. Kim, P. Liu, G. Kresse, and C. Franchini, Phys. Rev. Materials **2**, 024601 (2018).

[61] J. Mravlje, M. Aichhorn, and A. Georges, Phys. Rev. Lett. **108**, 197202 (2012).

[62] P. Pulay, Chemical Physics Letters **73**, 393 (1980).

Appendix A: Finite-size effects

Fig. 8 shows the finite-size effect for $SrVO_3$ and $SrMnO_3$. From 4×4×4 to 6×6×6, the total local DOS

becomes smoother and exhibits fewer features, while the general characteristics remain the same in both Brillouin zone discretizations, for both $SrVO_3$ and $SrMnO_3$.
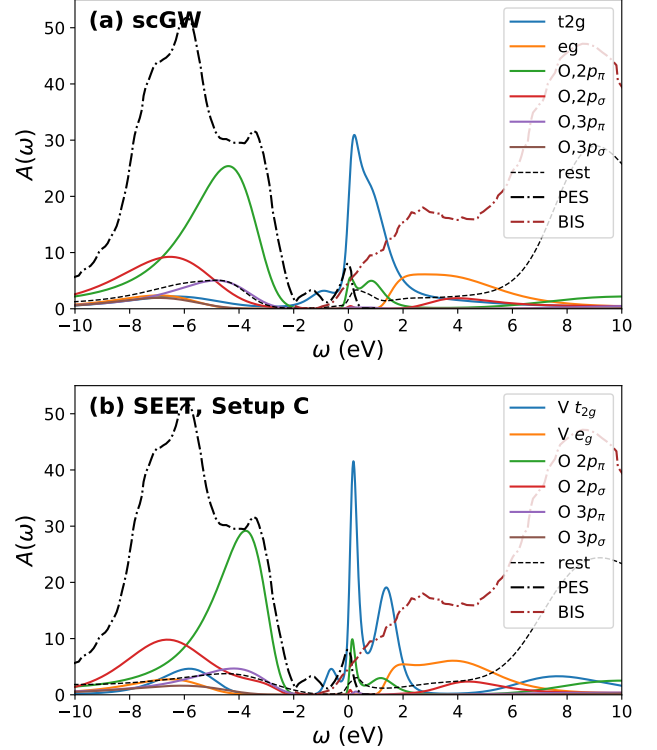
Appendix B: Basis set effect

Figure 9. Total local DOS for $SrVO_3$ from scGW and SEET. The impurity choices are setup C in Table I for $SrVO_3$ (The three peak structure for V t_{2g} quasiparticle peak in SEET is due to a coarser k-space discretization (4 × 4 × 4 k-points in the Brillouin zone).

In order to check whether the missing feature at ~ -1.5 eV may be due to a deficiency in our choice of Gaussian basis set, we have repeated the calculation with a larger basis for the vanadium atom in $SrVO_3$, *gth-tzvp-molopt-sr* [36]. As shown in Fig. 9, no qualitative difference was observed for vanadium in the *gth-tzvp-molopt-sr* basis, in both scGW and SEET calculations. This indicates that the absence of the feature is unlikely due to a deficiency of the vanadium basis.

Appendix C: G_0W_0 for $SrVO_3$

Fig. 10 shows the local DOS evaluated from G_0W_0 based on the LDA band structure. The G_0W_0 DOS looks qualitatively similar to the scGW results presented in Fig. 2 except for a slightly wider t_{2g} quasiparticle bandwidth. The hump between -1 and -2 eV is absent. Note
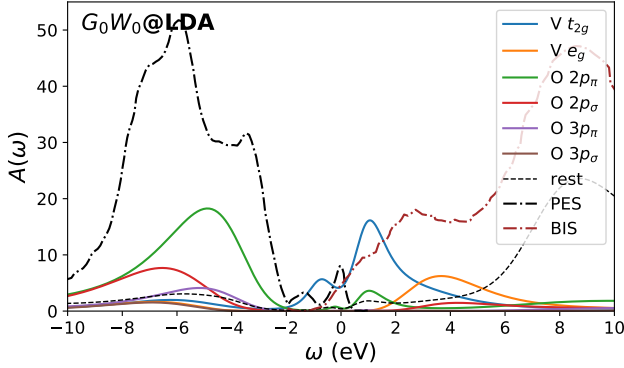
Figure 10. Total local DOS for $SrVO_3$ evaluated from G_0W_0 based on the LDA band structure.

that the double peak structure is due to the k-space discretization and is not a feature of a lower satellite.

Appendix D: Convergence of SrMnO₃

Fig. 11 shows SEET convergence of various quantities for SrMnO₃ with impurity choices specified in Setup B. Including local self-energy corrections from Mn $3d$ orbitals opens a gap in the first iteration. The system later oscillates between metallic and insulating states in the following iterations and slowly converged to the physical insulating phase. In order to facilitate the convergence, direct inversion of the iterative subspace (DIIS) [62] is employed after iteration 17 where much faster convergence is observed. Due to it, starting from iteration 17, we observe a much faster convergence.

Appendix E: SEET without outer-loop self-consistency for SrMnO₃

Fig. 12 shows local orbital-resolved DOS for SrMnO₃ from SEET without outer-loop self-consistency. The impurity choices are listed in Table. II. With non-perturbative treatments of the Mn t_{2g} orbitals, the DOS at E_F is greatly suppressed while still remaining non-zero (see the inset for Setup A in Fig. 12). In addition, an extra sharp quasiparticle peak from O $2p_\pi$ orbitals at around E_F is observed. Furthermore including the Mn e_g orbitals gives a similar qualitative picture as the one with only Mn t_{2g} orbitals. The only difference arises for the Mn e_g conduction band that is pushed forward to E_F, consistent with results from fully self-consistent SEET.

Next we include O $2p$ orbital in impurity setup C. Non-perturbative treatments to O $2p$ states push slightly valence bands away from E_F, making the sharp quasiparticle peak at E_F disappear. However, there is still non-zero DOS at E_F from O $2p$ states.

In general, although all three impurity choices employed greatly suppress DOS around E_F and qualita-
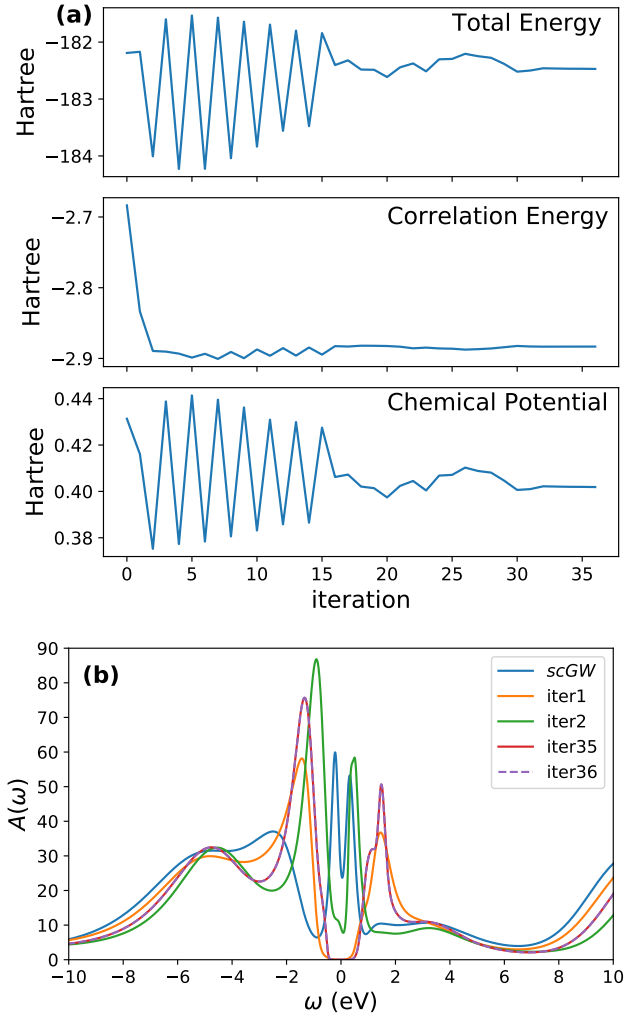

Figure 11. Convergence of (a) total energy, correlation energy, chemical potential, and (b) total local DOS for SrMnO₃ from SEET with impurity choices specified in Setup B.

tively predict correct orbital ordering in both valence and conduction bands, SrMnO₃ remains metallic with a small DOS at E_F. We argue that this unphysical metallic state is an artifact due to the lack of outer-loop self-consistency (the feedback of the strongly correlated orbitals to the weakly correlated part via the Dyson equation). Without the outer-loop self-consistency, weakly correlated orbitals outside the impurity subspaces cannot be adjusted by the correlations in the strongly correlated subspaces, resulting in incorrect chemical potential shifts.
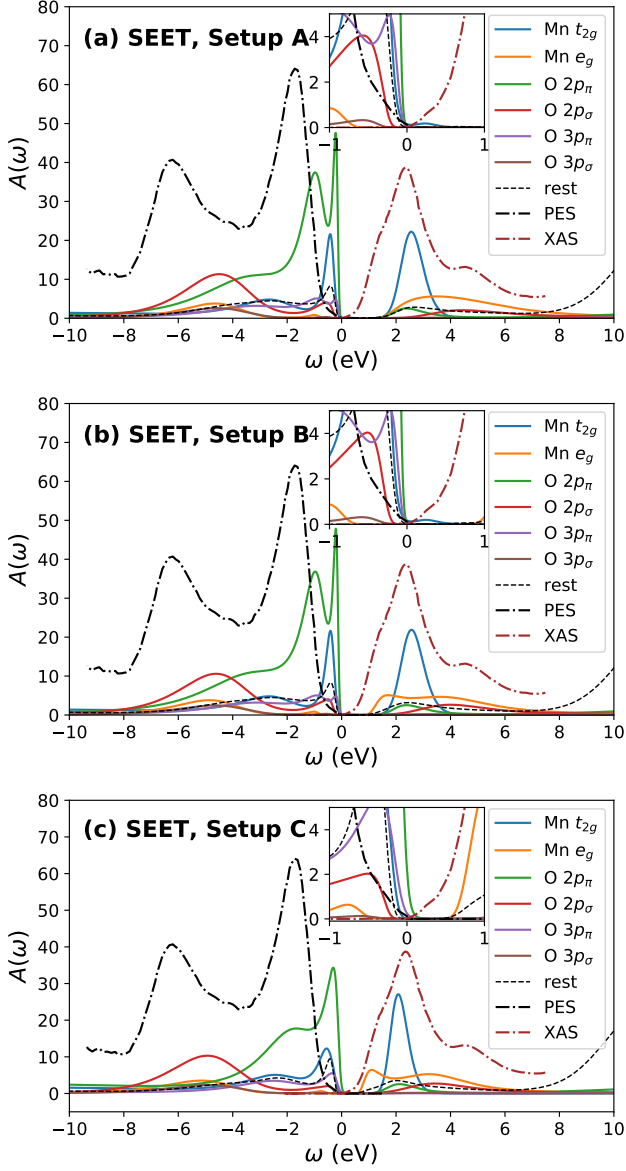
Figure 12. Orbital-resolved local DOS for SrMnO₃ from SEET without an outer-loop self-consistency. The impurity choices from the first to third row correspond to (A), (B), and (C) in Table II. The inset shows DOS around E_F. The dotted lines are photoemission data from ref [53].

Appendix F: SEET total density of states of SrMnO₃

Fig. 13 shows the SEET total local DOS of SrMnO₃. They are obtained by summing all orbitals. We found that the total DOS around the Fermi level is very similar to Fig. 6, which shows the sum of the local DOS of the Mn $3d$ + O $2p$ orbitals. The quantitative differences come from additional contributions of Mn $4d$ and O $3p$. The rest of orbitals mainly contribute to the lower/higher energy regime far away from the Fermi level.
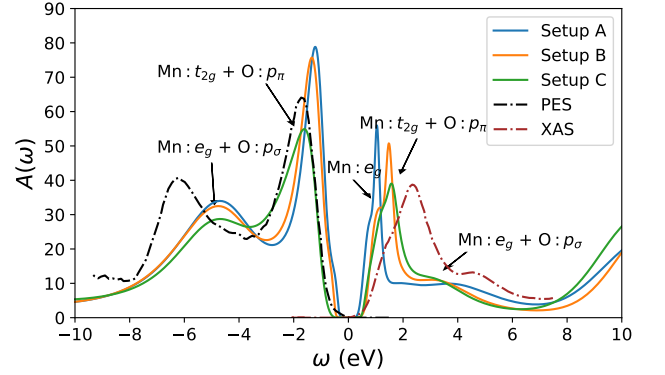

Figure 13. Total local density of states of SrMnO₃ from scGW and SEET with different impurity choices. Arrows indicate the orbital contributions according to SEET with impurity choice C. The PES and BIS data is obtained from Ref. [43, 44]